CrossMark

Coupling Effect of State-of-Health and State-of-Charge on the Mechanical Integrity of Lithium-Ion Batteries

J. Xu [1,2] · Y. Jia [1,2] · B. Liu [1,2] · H. Zhao [3,4] · H. Yu [3,4] · J. Li [3,4] · S. Yin [1,2]

Abstract

Two governing factors that influence the electrochemical behaviors of lithium-ion batteries (LIBs), namely, state of charge (SOC) and state of health (SOH), are constantly interchanged, thus hindering the understanding of the mechanical integrity of LIBs. This study investigates the electrochemical failure of LIBs with various SOHs and SOCs subjected to abusive mechanical loading. Comprehensive experiments on $LiNi_{0.8}CoO_{15}Al_{0.05}O_2$ (NCA) LIB show that SOH reduction leads to structural stiffness and that the change trend varies with SOC value. Low SOH, however, may mitigate this phenomenon. Electrochemical failure strain at short circuit has no relationship with SOC or SOH, whereas failure stress increases with the increase of SOC value. Experiments on three types of batteries, namely, NCA, $LiCoO_2$ (LCO), and $LiFePO_4$ (LFP) batteries, indicate that their mechanical behaviors share similar SOH-dependency properties. SOH also significantly influences failure stress, temperature increase, and stiffness, whereas its effect on failure strain is minimal. Results may provide valuable insights for the fundamental understanding of the electrochemically and mechanically coupled integrity of LIBs and establish a solid foundation for LIB crash-safety design in electric vehicles.

Introduction

Lithium-ion batteries (LIBs), owing to their excellent performance due to their high specific power and energy densities, have become increasingly employed for various applications, including cellphones [1, 2], laptops [2], and electric vehicles (EVs) [3–9]. With the recent tremendous expansion of the EV and hybrid EV market [10, 11], inevitable vehicle crash accidents now pose severe threats to the society with the possible burning or explosion of LIB-based systems [12]. The mechanical integrity of LIBs has therefore captured the interest of scientists and engineers from the fields of electrochemistry, material science, and mechanics, thereby becoming a hot research topic.

Pioneering work on the mechanical integrity of LIBs started with classical mechanical analysis that considered the LIB cell as a structure containing various materials and components [13–17] and numerical simulation to study the stress and strain evolution of LIB cells during abusive mechanical loadings [16, 18–23]. Various loading conditions, such as radial compression [16, 17, 22], indentation [16, 18], and bending [16, 19], on fully drained LIBs with low state of charge (SOC), were employed to mimic real-world loadings to understand mechanical–electrochemical behaviors [16, 17, 21, 22]. The quantitative onset of short-circuit criteria was also determined on the basis of the mechanical behaviors of LIBs to assist mechanical integrity [16].

However, due to the continuous charge/discharge cycles of batteries, the SOC and state of health (SOH) of LIBs constantly vary, which leads to different stress statuses within the cell [24, 25]. Theoretical [26–29] and experimental studies [30–32] on silicone anodes revealed that the insertion of lithium ion can cause elastic softening of the anode. Recent evidences demonstrated that the mechanical properties [33, 34] and volumes [35] of the active particles change because of varying SOC values. By contrast, other studies indicated that

✉ S. Yin
  shayin@buaa.edu.cn

1 Department of Automotive Engineering, School of Transportation Science and Engineering, Beihang University, Beijing 100191, China

2 Advanced Vehicle Research Center (AVRC), Beihang University, Beijing 100191, China

3 Chongqing Changan Automobile Co. Ltd., Chongqing 400023, China

4 State Key Laboratory of Vehicle NVH and Safety Technology, Chongqing 401120, China

the battery electrodes [36–39] and the current collector [40] change in morphology and structure during battery life cycle. To further accurately describe and predict the electrochemically dependent mechanical behaviors of LIBs subjected to abusive mechanical loadings, the quantitative relationships between SOC status and mechanical behaviors were determined through experiments [41]. A dynamic mechanical model [42] with the coupling of strain rate and SOC effects [43, 44] was also established. However, the life cycle of LIBs and the coupling effect that caused SOC and SOH were not considered.

To bridge this gap, this study investigates the mechanical integrity behavior of LIBs under different SOH and SOC values by selecting 18,650 LIBs as target cells. Load, voltage, and temperature are monitored and recorded over time. Governing parameters that characterize the mechanical integrity of LIBs are summarized, compared, and analyzed at different SOCs and SOHs and among different types of LIBs.

This paper is organized as follows. Second section describes the experimental methods, including experimental samples, characterization method, and experimental design. Third section presents the typical result for NCA batteries. Forth section discusses the experimental results on the three types of batteries.

Methods

Experimental Samples

Several widely commercialized 18,650 LIBs were selected as target cells, as shown in Fig. 1(a). These cells were supplied by Sony (LCO cell), Panasonic (NCA cell), and Lishen (LFP cell). The nominal capacities, nominal voltages, and charge cutoff voltages of these 18,650 LIBs are listed in Table 1.

These cells mainly consist of shell, jellyroll, and mandrel. The cylindrical jellyrolls are wound with two layers of separator, one layer of positive electrode, and another layer of negative electrode.

Experimental Method

Large-deformation compression tests were performed to mimic the possible abusive external mechanical loadings imposed on LIBs. The loading rate was set at 2 mm/min to provide quasi-static mechanical loadings, where strain rate and inertia effects were excluded. During loadings, the displacement, load, voltage, surface temperature of batteries, and environmental temperature were recorded in real time.

Figure 1(b) and (c) provide the schematic illustration of the compression test. Open-circuit voltage was measured by connecting the sensor joints to the positive and negative of the sample battery. The temperature measurement points were located on the cell surface along the middle of the axis, where minimal deformation occurred. Fair comparison of

temperature changes in various testing samples with different heat capacities was initially ruled out due to the small changes in laboratory temperature during the experiment.

To better describe the mechanical integrity behaviors of target LIBs, we introduced two parameters, namely, nominal strain and stress, which are similar to those in a previous study [41], to describe the mechanical behavior of LIBs. Failure stress and strain emerge when internal short circuit is triggered.

The nominal strain is equal to the displacement/diameter ratio, which can be expressed as follows:

$$\varepsilon_n = \frac{d}{2R}, \tag{1}$$

where d is the displacement of the compression plate and R is the radial of the battery, as shown in Fig. 1(d). The nominal stress is equal to the load/contact area ratio, which can be expressed as follows:

$$\sigma_n = \frac{F}{S_c}, \tag{2}$$

where F is the force and S_c is the contact area. The product of the length and contact width of LIBs can be used to express varying contact areas, as follows:

$$S_c = l_c b_c, \tag{3}$$

where l_c is the cell length, which is constant; and b_c is the contact width, which changes with the displacement, as shown in Fig. 1(d). b_c is calculated as follows:

$$b_c = 2R \arccos\left(\frac{R - d/2}{R}\right) \tag{4}$$

INSTRON 8801 universal material testing machine (Fig. 1(c)) was used as the mechanical testing platform for compression tests with a maximum load of 10 kN and an enhanced resolution of 50 N. Accuracy refers to the maximum of ±5% of the set value and 0.005% of the load cell capacity. The LIB voltage was measured in situ by Agilent 34410A digital voltmeter with a recording frequency of 20 Hz and an accuracy of 0.01 mV. The LIB surface temperature was measured in situ by ANBAI AT4508 multi-channel temperature sensors and K-type thermocouples. The measurement range is 200 °C–1300 °C, and the resolution ratio is 0.1 °C. The recording frequency is 1 Hz, and the accuracy is 0.2 °C. BK6808AR rechargeable battery performance testing equipment with a controlling computer was used to prepare battery test samples.

Experimental Design

Charge/discharge cycles were used to characterize SOH status. The main influencing factor of SOH was generally the
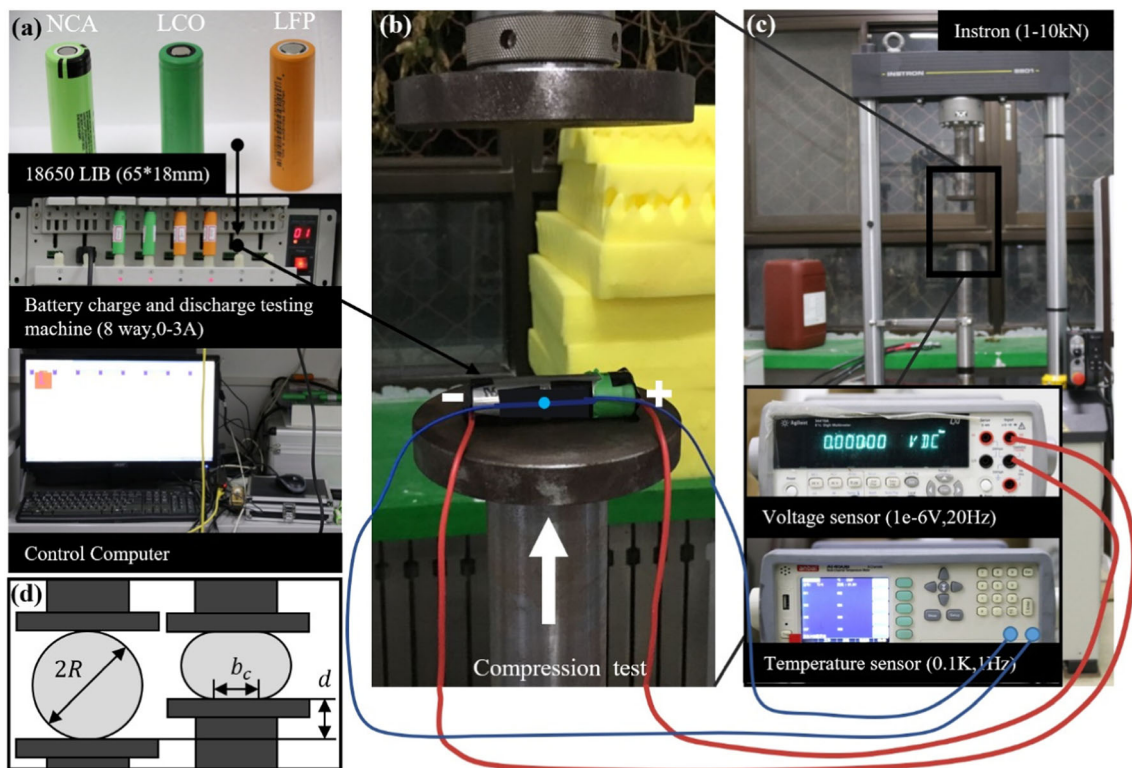
Fig. 1 Schematic illustrations of experimental setups: (**a**) three types of 18,650 LIB cell samples, battery charge and discharge testing machine, and the control computer, (**b**) compression test, (**c**) experimental devices, including universal material testing machine, voltage sensor, and temperature sensor, (**d**) deformation of 18,650 LIB cells during the compression test

cycles, and evidence showed the relationship of the SOH and SOC values. The SOH value, defined as the ratio of residual capacity and initial capacity, decreases as cycles increase [45–48]. We used cycles to characterize the SOH, as shown in Fig. 2(a), and ruled out the possibility that laboratory temperature may lengthen the battery cycle experiment. The SOC value, defined as the ratio of input capacity and nominal capacity, was accurately controlled through the battery performance testing equipment.

We selected brand-new batteries and used a battery performance testing equipment to charge and discharge them to the required cycles. The cycle test mode is in constant current in order not to introduce more influencing factors. We selected a 0.5 C cycle rate considering the

efficiency and safety of the tests. The charge and discharge cutoff voltages are shown in Table 1. The charge/discharge curve is shown in Fig. 2(b). The cells were charged with a constant current to the designated SOC value at 0.5 C. The prepared sample descriptions with testing matrix are presented in Table 2. We performed four test repetitions for each experiment scenario due to the inconsistency among testing battery samples. Forty experiments were conducted. The experiments had excellent repeatability from the perspective of mechanics, as shown in Fig. 2(c).

We adopted the small-cycle and large-rate experimental method to mimic the varying SOH conditions. For example, the normal working current of the selected NCA batteries is

Table 1 List of specifications for the 18,650 LIB test samples

LIB system	NCA	LCO	LFP
Manufacturer	Panasonic	Sony	Lishen
Type	NCR 18650-B	18,650	LS-LR18650EC
Discharge cutoff voltage (V)	2.5	2.5	2.0
Cathode/anode materials	$LiNi_{0.8}Co_{0.15}Al_{0.05}O_2$ /graphite	$LiCoO_2$/graphite	$LiFePO_4$/graphite
Nominal voltage (V)	3.7	3.7	3.2
Nominal capacity (mAh)	3350	2250	1350
Max charge/discharge current (C)	0.5/1.5	1/10	0.5/1

Fig. 2 (a) SOH-cycle curve at 0.5 C of NCA battery, (b) Charge/discharge curve at 0.5 C of NCA battery, (c) Load-displacement curves of four NCA batteries with SOC = 0 and 1 cycle
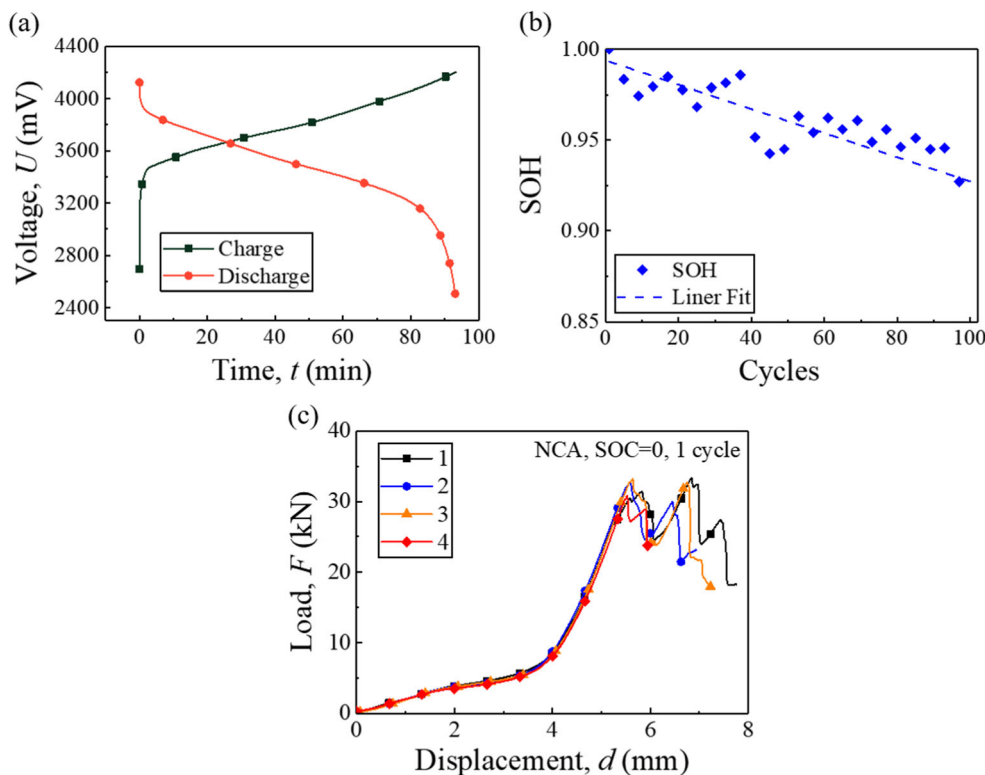
0.1 C–0.2 C, and the normal capacity is 3400 mAh; therefore, a 0.5 C cycle rate indicates a high utilization intensity. To save time, the charge/discharge cycles are set as 1, 10, 50, and 100.

Results

Figure 3 shows that the stress σ_n first increases gradually because of the possible gaps among battery skin and the jellyroll, layers in the jellyroll, and the central mandrel. Furthermore, σ_n flows into a plateau when the internal mandrel buckles. The battery gradually becomes dense when the clearances among the layers are eliminated. As the structure becomes stiffer, σ_n increases drastically. Once the electrodes and separator layers of the jellyroll fracture completely, stress evidently decreases. The force decreases at $\varepsilon_n = 0.309$ ($d = 5.56$ mm) mainly due to the large-scale fracture in the jellyroll.

Table 2 Cycling procedure and conditions for the pulsed discharged cells

Type	Cycle rate	Method	Cycles	SOC
NCA	0.5 C	Constant current	1, 10, 50, 100	0, 0.4
LCO	0.5 C	Constant current	1, 10, 100	0.4
LFP	0.5 C	Constant current	1, 10, 100	0.4

The voltage also increases slightly from 3.328 V up to 3.354 V in the loading before the onset of battery short circuit. After reaching Maximum Point A (Fig. 3), the voltage begins to decrease slightly because the internal micro short circuit is triggered. After the mechanical fracture of Point B, the voltage decreases drastically because the jellyroll is fractured. The initial room temperature is 17 °C. The temperature increase was measured to obtain an indirect evidence of battery failure. Naturally, the surface temperature change ΔT monitoring on the cell is almost constant before the internal short circuit. Once short circuit starts, the temperature begins to rise and reaches its peak value after approximately 30 s. A low SOC value causes the low temperature increase, and the thermal runaway is not triggered. The lag in temperature increase in contrast with the voltage decrease is mainly caused by the low-frequency data recording and the heat propagation time from the short-circuit point to the cell surface.

The $d\sigma_n/d\varepsilon_n$ curve profile shown in Fig. 3 exhibits roughly the same trend as the stress–strain curve profile. When $d\sigma_n/d\varepsilon_n$ reaches its peak value, the internal micro short circuit occurs (Point A), and the voltage starts to decrease slightly. Local temperature increase softens the cell material, thus accelerating the thermal buckling of cell materials. The bulking causes the loss of battery bearing capacity and softens the structural stiffness of the battery. The battery skin then starts to fracture, $d\sigma_n/d\varepsilon_n$

Fig. 3 Typical mechanical and electrochemistry behaviors in compression loadings, including stress–strain, voltage–strain, temperature–strain, and derivative nominal stress–strain curves, during the compression test with a deformation rate of 2 mm/min for 18,650 lithium-ion battery at SOC = 0
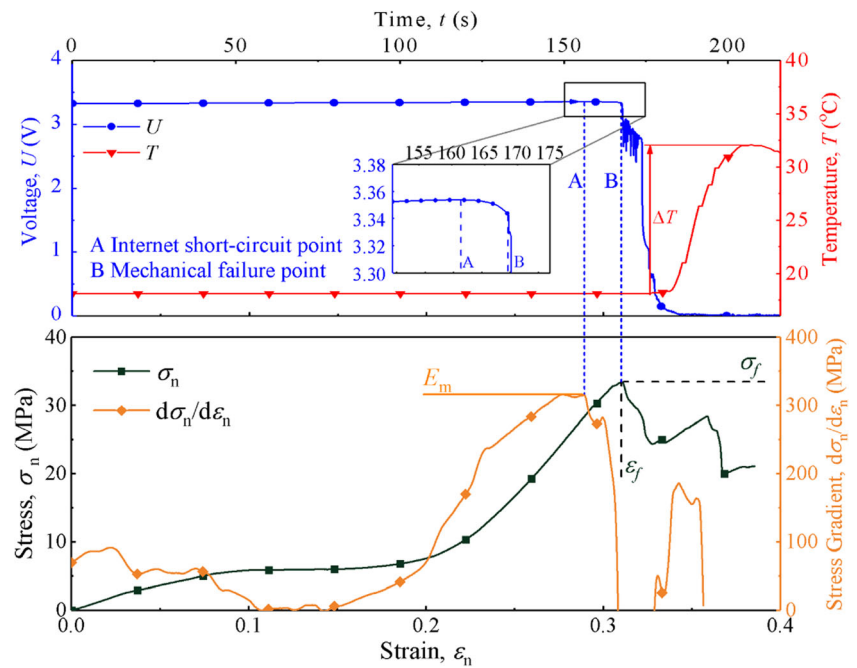
decreases drastically, and the jellyroll starts to bear the loadings. At approximately 0.309 strain (5.56 mm displacement), a large portion of the layer fractures, thus causing a large drop in $d\sigma_n/d\varepsilon_n$, and the voltage drops to zero (Point B). The $d\sigma_n/d\varepsilon_n$ value in Point A can be extracted (shown as tangent modulus E_m in Fig. 3, the maximum value of $d\sigma_n/d\varepsilon_n$ before the failure of the battery). The failure strain ε_f and failure stress σ_f can be extracted from Point B.

Batteries with different material systems may differ slightly in mechanical behaviors due to the differences in the battery shell thickness, cathode or anode material properties, capacity, and processing technology of the battery.

On the one hand, the tangent module reflects the differences in the initial liner phase. The tangent module in the initial liner phase for the NCA battery is approximately 68.4 MPa, and the corresponding strain variation is 0.084. However, for the LCO and LFP batteries, the tangent module values are 227.0 MPa and 274.6 MPa, and the strain variations are 0.036 and 0.025, respectively. The selected LFP and LCO batteries have thicker shells than that of the NCA battery. The thickness t of NCA, LCO, and LFP battery shells are 0.15, 0.25, and 0.3 mm, respectively. Assuming that the battery shell is for a thin wall cylinder and a small deformation occurs during loading, length L and the inertia moment of the shell $I_z = Lt^3/12$. Therefore, the displacement d of the functional point of F equals

$$d = \int_0^\pi \int \frac{RF\sin(\alpha)}{2EI_z}\cos(\alpha) = \frac{ELFt^3}{6\pi R^2}, \tag{5}$$

where R is the shell radius and E is the elastic module of shell. Therefore,

$$\frac{d}{F} = \frac{ELt^3}{6\pi R^2} \propto t^3. \tag{6}$$

When t increases, the equivalent stiffness of the thin wall and the initial tangent modulus increase. This condition is mainly exhibited in the first half part of the curves in Fig. 4, where LCO and LFP batteries exhibit higher overall stiffness than NCA batteries. On the other hand, the densification strain reflect the differences. The densification strain (inflection point of $d\sigma_n/d\varepsilon_n$) of the NCA, LCO, and LFP batteries are approximately 0.198, 0.220, and 0.208, respectively, as shown in Fig. 4. The nominal capacities of the three types of batteries are 3350, 2250, and 1350 mAh, respectively. The NCA batteries have higher capacities and more compact internal structures, thus causing a shorter period of force plateau in the stress–strain curve, smaller densification strain, and failure strain.

Discussions

SOH-Dependent Mechanical Integrity Behavior

To investigate the relationship between SOH and mechanical integrity behavior, we selected a set of NCA 18650 LIBs with SOC = 0 and 1, 10, 50, and 100 cycles. Fig. 5(a) shows that the overall profiles at various cycles are similar, but the structural stiffness increases with the increase of charge/

Fig. 4 Different mechanical behaviors of LCO, LFP, and NCA 18650 LIBs at SOC = 0.4, 1 cycle during compression tests: nominal stress–strain curves and derivative nominal stress–strain curves
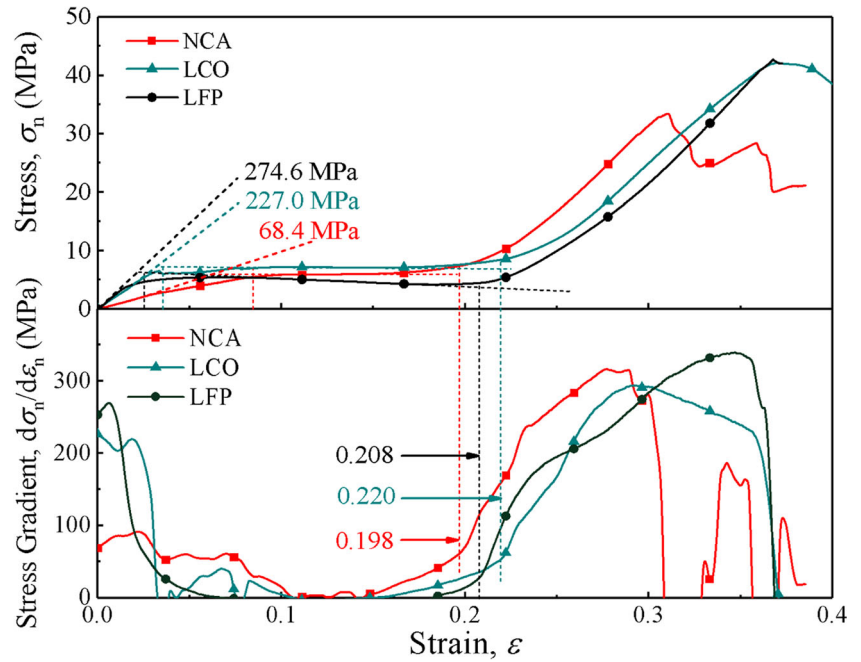
discharge cycles until the sudden force/nominal stress decreases. In other words, used batteries may share the same
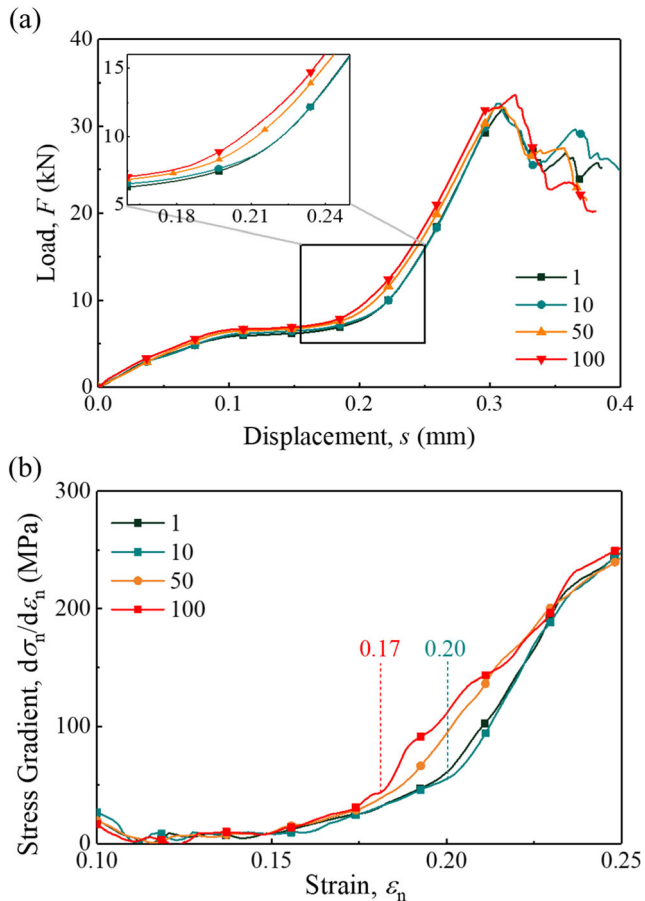

Fig. 5 Mechanical behavior curves of NCA LIBs at SOC = 0 in various cycles: (**a**) load–displacement curve, (**b**) stress gradient curve

mechanical behaviors but exhibit high structural stiffness. The $d\sigma_n/d\varepsilon_n$ curves shown in Fig. 5(b) demonstrate that the stiffness increase is large for batteries with more cycles. For 100 cycles, this "hardening effect" is more evident, and the cell may enter densification stage (inflection point of $d\sigma_n/d\varepsilon_n$) at a displacement of 3.5 mm or $\varepsilon_n \approx 0.17$, whereas the cell with 1 cycle becomes fully densified at 4.5 mm or $\varepsilon_n \approx 0.20$. The decrease of densification strain means the thickening of the electrode layers after repeated cycles [49].

As shown in Fig. 6, the maximum stiffness E_m remains unchanged with the cycle increase. As the cycles increase, ΔT also gradually increases, indicating a deteriorated thermal condition. ε_f decreases slightly and σ_f increases as the cycles increase.

As the cycles increase, the structure and composition of electrode materials change. The phase change of cathode [50], the loose structure of anode [51], and the lithium deposits [49] may increase the structural stiffness and temperature rise. Within 100 cycles and SOC = 0, the ageing effects of separator cause the slight decline of ε_f. The increase of structural stiffness also leads to the increase of σ_f. The separator is the key component to maintain the electrochemistry performance of the battery. The separator thus determines the capability to prevent the short circuit.

Comparison Among the Different Batteries (NCA, LCO, and LFP)

To explore the SOH-dependent mechanical integrity behaviors in 18,650 LIBs, we selected three types of 18,650 LIBs, namely, NCA, LFP, and LCO, for the compression experiment under the same condition. The SOC is 0.4, and the cycles are 1, 10, and 100.

As shown in Fig. 7, the trends of E_m for the three types of batteries are similar. E_m monotonically declines

Fig. 6 (**a**) Tangent modulus–cycle, (**b**) temperature rise–cycle, (**c**) failure strain–cycle, and (**d**) failure stress–cycle curves for different NCA LIBs at SOC = 0
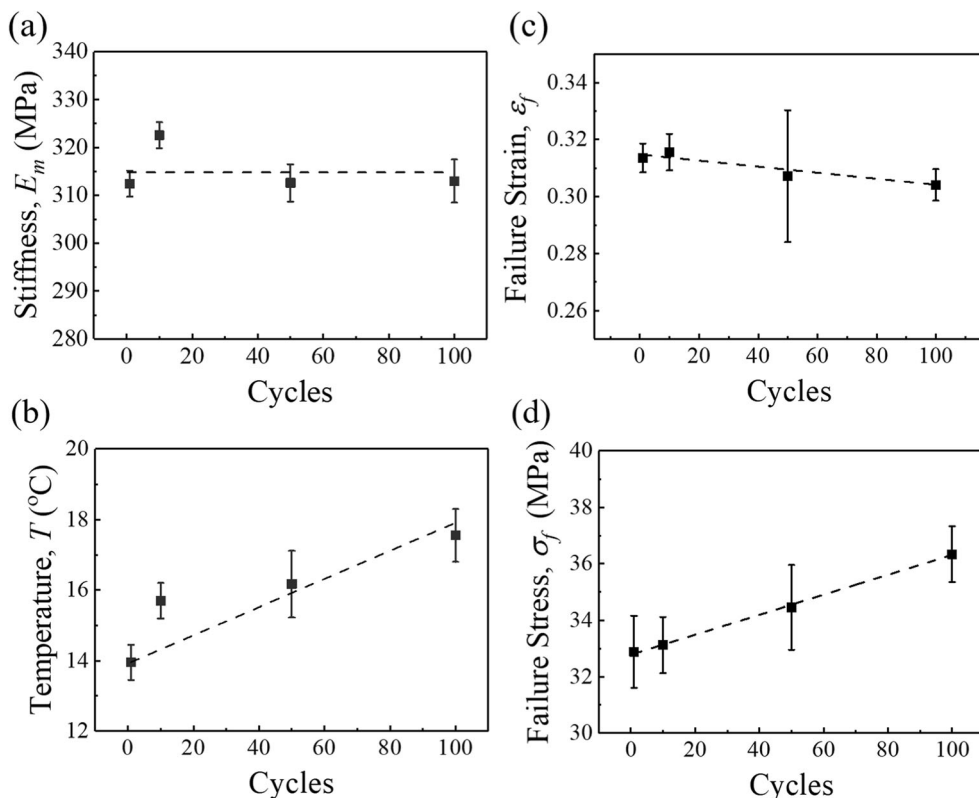
with the increase of cycles in the three groups. Among the three types of batteries, the LFP battery has the maximum amplitude of drop, and the change ranges of the NCA and LCO batteries are smaller.

Fig. 7 Mechanical, electrochemistry, and failure behaviors of LCO, LFP, and NCA LIBs at SOC = 0.4 in various cycles, in terms of (**a**) maximum structural stiffness–cycle, (**b**) temperature rise–cycle, (**c**) failure strain–cycle, and (**d**) failure stress–cycle curves
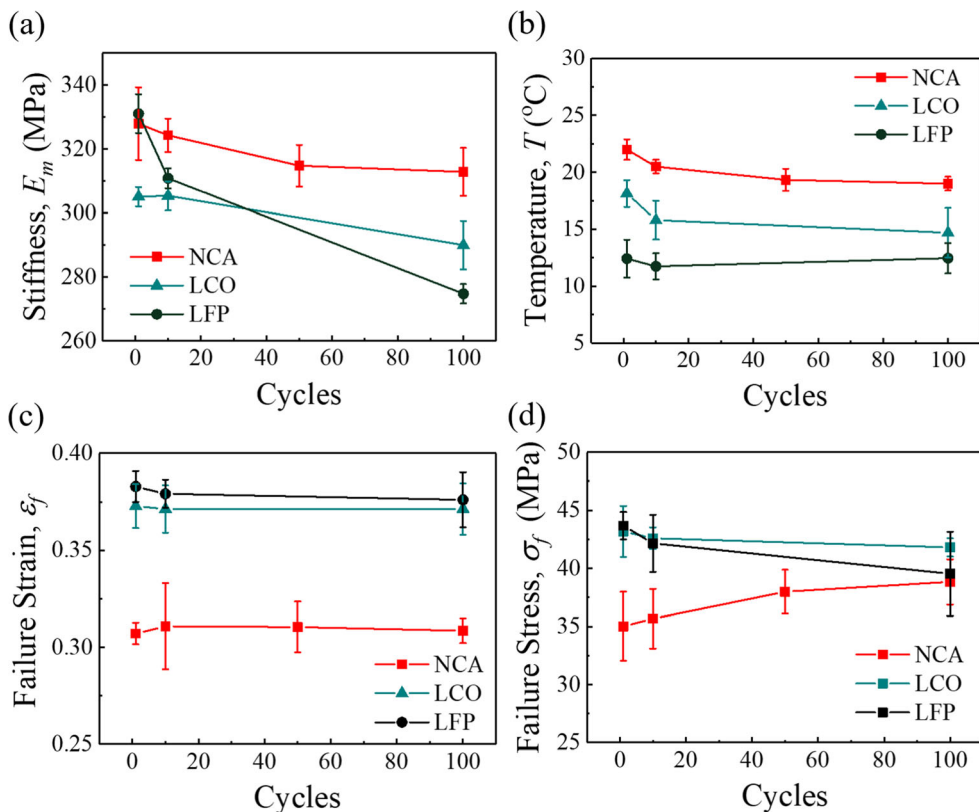
ΔT decreases slightly with the addition of cycles. The decrease ranges of NCA and LCO batteries are larger than that of the LFP battery. The ΔT of the LFP battery is constant. By contrast, the high capacity of the battery model may lead to high ΔT.

The ε_f and σ_f of the LCO and LFP batteries have different tendencies compared with those of NCA batteries. ε_f and σ_f monotonically decline with increasing cycles of LCO and LFP batteries. The difference among the three types of batteries is caused by the different material systems (including the shells), nominal capacities, and manufacturing processes.

Considering the influence of manufacturing process, material system, and other factors, different types of batteries may have different change trends. Among these parameters, the influence of the cycles is least on ε_f, as shown in Fig. 8.

SOC-Dependent Mechanical Integrity Behavior

A group of NCA LIBs with SOC = 0 and 0.4 with 1 charge/discharge cycle was selected for the experiment under the same condition to determine SOC-dependent mechanical integrity behavior. The stiffness of high-SOC batteries is generally greater than the stiffness of low-SOC batteries, as shown in two typical curves in Figs. 9(a) and (b). Quantitatively similar results on LCO LIBs were reported by Ref. [41]. Thus, different types of LIBs share similar SOC-hardening behaviors.

Results show that the variation of SOC value from SOC = 0 to 0.4. E_m increased by 6.27%; ΔT increased by approximately 49.06% because a battery with a high SOC value may carry more energy; ε_f did not change with SOC; and σ_f increased by over 6.51%.
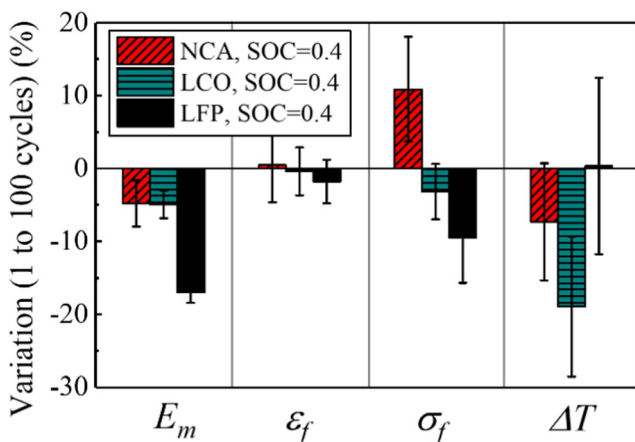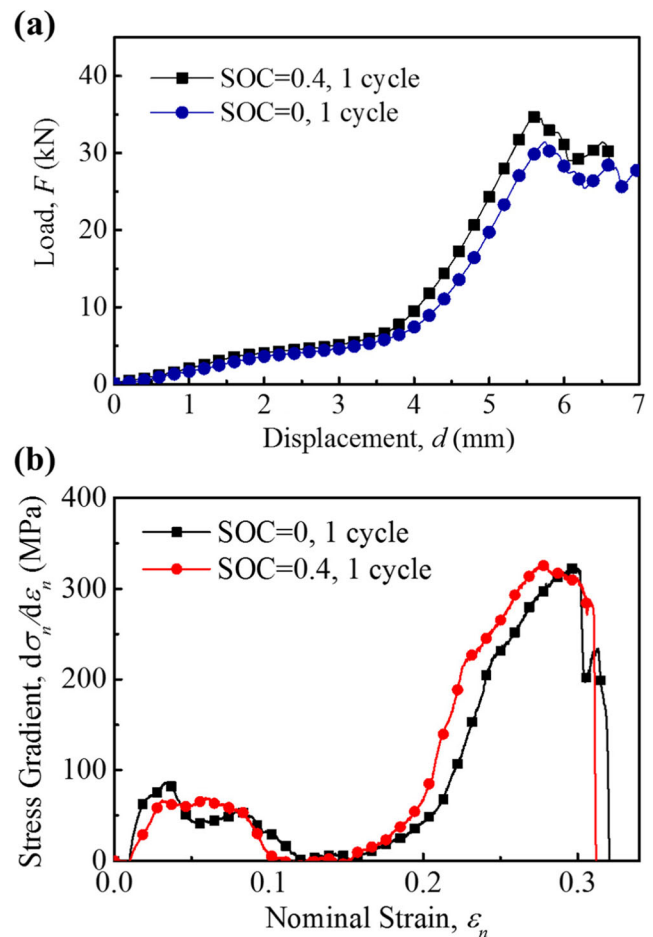
Fig. 9 (a) Load–displacement and (b) nominal stress–strain curves of NCA LIBs at SOC = 0 and 0.4

The increase of E_m is caused by the insertion of Li$^+$, which further causes the initial stress of the graphite anode and stiffens the structure [52]. Therefore, the temperature rise increases significantly as compared with that of low-SOC batteries. Owing to the stiffer structure, σ_f also increases.

Coupling Effect of SOH and SOC on LIB Mechanical Behaviors

To further explore the coupling effect brought about by SOH and SOC, we selected a group of NCA LIBs with SOC = 0/0.4 and 1, 10, 50, and 100 cycles. All cells generally exhibited similar mechanical response, as shown in Fig. 10(a). The peak forces F are greater when SOC increases, and F increases slightly with the increase in cycles, as shown in Fig. 10(b).

For the batteries, the percentage of E_m increases from SOC = 0 to 0.4 as cycles decrease, but the variation decreases slowly, as shown in Fig. 10(c). As the cycle increases, the stiffness decreases at SOC = 0.4 and increases slightly at SOC = 0. By contrast, the capacity

Fig. 8 Variation of four main parameters for the three types of LIBs from 1 to 100 cycles

Fig. 10 (**a**) Load–displacement, (**b**) maximum load–cycle, (**c**) percentage of tangent module increase (from SOC = 0 to 0.4)–cycle, (**d**) temperature rise–cycle, (**e**) failure strain–cycle, and (**f**) failure stress–cycle curves of different NCA LIBs at SOC = 0 and 0.4 under different cycles
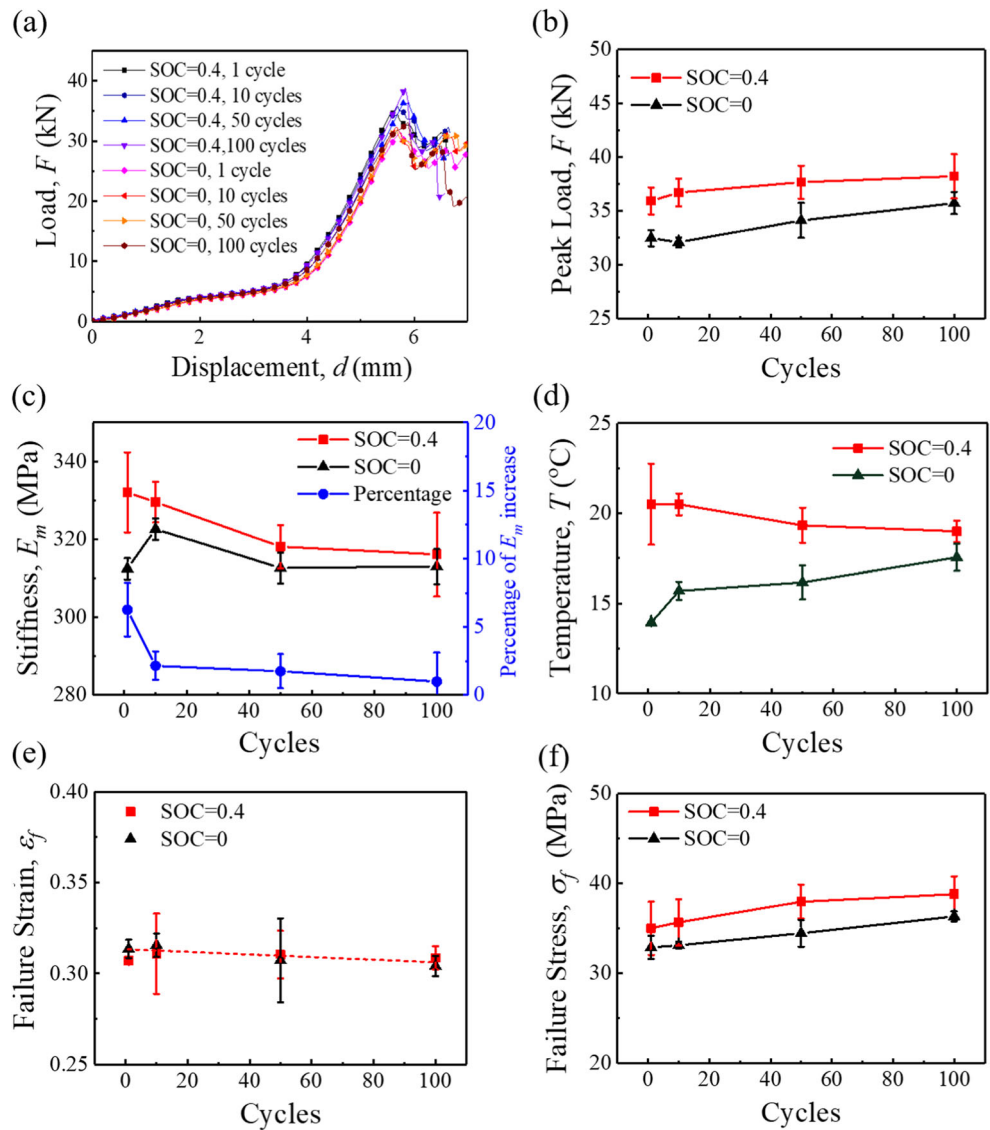
is lost, and the charging efficiency decreases as the cycles increase. Those conditions reduce the SOC-hardening effect.

As the cycles increase, ΔT increases when SOC = 0 and decreases when SOC = 0.4, as shown in Fig. 10(d). As the cycles increase, the difference in ΔT is gradually narrowed between the LIB group with SOC = 0 and 0.4.

As shown in Figs. 10(e) and (f), ε_f is quite stable in various SOC and SOH statuses because the structural stiffness hardening effects would be compensated by the high failure stresses with high SOCs and cycles. σ_f increases. This process is caused by the SOH stiffness effects, as mentioned above.

Table 3 summarizes the effects caused by various SOCs and SOHs. In general, the increase of SOC also renders the effect of cycles on the mechanical integrity behaviors less evident for NCA 18650 LIBs, as shown in Fig. 11. This

finding can be attributed to the impact of SOH, which is mainly reflected in the battery anode. The coupling effect of SOC and SOH indicates that the electrochemical status significantly influences the mechanical integrity of LIBs.

Table 3 Variation trend of mechanical integrity behaviors in NCA LIBs at SOC = 0/0.4 and various SOH values during compression tests

NCA(Cycles)	SOC = 0	SOC = 0.4	Comparison of SOC = 0 and SOC = 0.4
Maximum structual stiffness	↑*	↓	<
Failure strain	→	→	≅
Failure stress	↑	↑	<
Temperature rise	↑	↓*	<

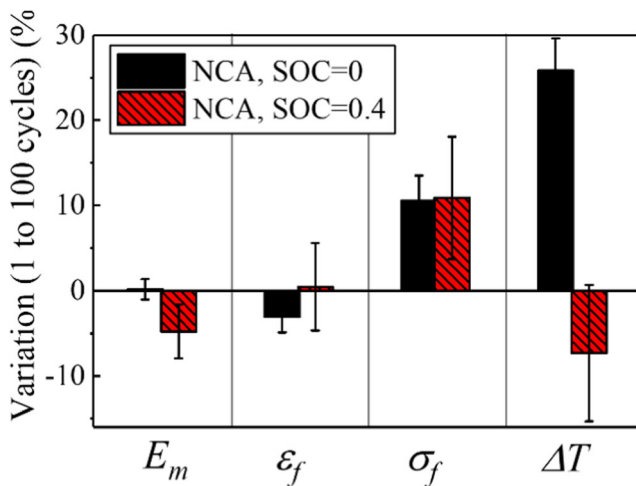Legend: ↑ Increase ↓ Decrease * Slightly → Unchanged

Fig. 11 Variation of different NCA LIBs at SOC = 0 and 0.4 after 100 cycles by comparison of corresponding cells after 1 cycle

Concluding Remarks

The SOC and SOH are two critical factors affecting the mechanical integrity behavior of LIBs, especially the coupling effect of SOH and SOC with charge/discharge cycles. This study investigated the SOH/SOC-dependent mechanical integrity behaviors of NCA LIBs and the SOH-dependent mechanical integrity behaviors of the three types of widely commercialized 18,650 LIBs in compression tests. The coupling effects of SOH and SOC were also investigated. Experiments on NCA LIBs show that SOH reduction leads to structural stiffness and that the change trend varies with SOC value. Failure deformation at short circuit has no relationship with the SOC or SOH value, whereas failure stress increases with the increase of SOC value. Experiments on the three types of battery indicate that different types of batteries may have similar SOH-dependent mechanical behaviors. SOH slightly affects failure the strain and significantly influences the failure stress, temperature increase, and stiffness.

Results may provide valuable insights for understanding electrochemical mechanisms as working conditions for the mechanical integrity of LIBs and establish a solid foundation for LIB crash-safety design in EVs.

References

1. Armand M, Tarascon JM (2008) Building better batteries. Nature 451(7179):652–657

2. Scrosati B, Garche J (2010) Lithium batteries: status, prospects and future. J Power Sources 195(9):2419–2430

3. Chan CK, Peng H, Liu G, McIlwrath K, Zhang XF, Huggins RA, Cui Y (2008) High-performance lithium battery anodes using silicon nanowires. Nat Nanotechnol 3(1):31–35

4. Kang B, Ceder G (2009) Battery materials for ultrafast charging and discharging. Nature 458(7235):190–193

5. Sun Y-K, Myung S-T, Park B-C, Prakash J, Belharouak I, Amine K (2009) High-energy cathode material for long-life and safe lithium batteries. Nat Mater 8(4):320–324

6. Goodenough JB, Kim Y (2010) Challenges for rechargeable li batteries. Chem Mater 22(3):587–603

7. Cheng F, Liang J, Tao Z, Chen J (2011) Functional materials for rechargeable batteries. Adv Mater 23(15):1695–1715

8. Vikström H, Davidsson S, Höök M (2013) Lithium availability and future production outlooks. Appl Energy 110:252–266

9. Ovrum E, Bergh TF (2015) Modelling lithium-ion battery hybrid ship crane operation. Appl Energy 152:162–172

10. Chen J, Liu J, Qi Y, Sun T, Li X (2013) Unveiling the roles of binder in the mechanical integrity of electrodes for lithium-ion batteries. J Electrochem Soc 160(9):A1502–A1509

11. Ramdon S, Bhushan B (2014) Nanomechanical characterization and mechanical integrity of unaged and aged Li-ion battery cathodes. J Power Sources 246:219–224

12. Wang Q, Ping P, Zhao X, Chu G, Sun J, Chen C (2012) Thermal runaway caused fire and explosion of lithium ion battery. J Power Sources 208:210–224

13. Zhang X, Shyy W, Marie Sastry A (2007) Numerical simulation of intercalation-induced stress in Li-ion battery electrode particles. J Electrochem Soc 154(10):A910–A916

14. Golmon S, Maute K, Dunn ML (2009) Numerical modeling of electrochemical–mechanical interactions in lithium polymer batteries. Comput Struct 87(23–24):1567–1579

15. Cai L, White RE (2011) Mathematical modeling of a lithium ion battery with thermal effects in COMSOL Inc. Multiphysics (MP) software. J Power Sources 196(14):5985–5989

16. Greve L, Fehrenbach C (2012) Mechanical testing and macromechanical finite element simulation of the deformation, fracture, and short circuit initiation of cylindrical Lithium ion battery cells. J Power Sources 214:377–385

17. Sahraei E, Meier J, Wierzbicki T (2014) Characterizing and modeling mechanical properties and onset of short circuit for three types of lithium-ion pouch cells. J Power Sources 247:503–516

18. Sahraei E, Campbell J, Wierzbicki T (2012) Modeling and short circuit detection of 18650 Li-ion cells under mechanical abuse conditions. J Power Sources 220:360–372

19. Sahraei E, Hill R, Wierzbicki T (2012) Calibration and finite element simulation of pouch lithium-ion batteries for mechanical integrity. J Power Sources 201:307–321

20. Ali MY, Lai WJ, Pan J (2013) Computational models for simulations of lithium-ion battery cells under constrained compression tests. J Power Sources 242:325–340

21. Wierzbicki T, Sahraei E (2013) Homogenized mechanical properties for the jellyroll of cylindrical Lithium-ion cells. J Power Sources 241:467–476

22. Lai W-J, Ali MY, Pan J (2014) Mechanical behavior of representative volume elements of lithium-ion battery cells under compressive loading conditions. J Power Sources 245:609–623

23. Ali MY, Lai WJ, Pan J (2015) Computational models for simulation of a lithium-ion battery module specimen under punch indentation. J Power Sources 273:448–459

24. Cannarella J, Arnold CB (2014) State of health and charge measurements in lithium-ion batteries using mechanical stress. J Power Sources 269:7–14

25. Cannarella J, Leng CZ, Arnold CB (2014) On the coupling between stress and voltage in lithium-ion pouch cells. Proc of SPIE 9115:91150K

26. Obrovac MN, Christensen L (2004) Structural changes in silicon anodes during lithium insertion/extraction. Electrochem Solid-State Lett 7(5):A93–A96

27. Zhao K, Pharr M, Cai S, Vlassak JJ, Suo Z (2011) Large plastic deformation in high-capacity lithium-ion batteries caused by charge and discharge. J Am Ceram Soc 94:s226–s235

28. Liu XH, Wang JW, Huang S, Fan F, Huang X, Liu Y, Krylyuk S, Yoo J, Dayeh SA, Davydov AV, Mao SX, Picraux ST, Zhang S, Li J, Zhu T, Huang JY (2012) In situ atomic-scale imaging of electrochemical lithiation in silicon. Nat Nanotechnol 7(11):749–756

29. Pharr M, Zhao K, Wang X, Suo Z, Vlassak JJ (2012) Kinetics of initial lithiation of crystalline silicon electrodes of lithium-ion batteries. Nano Lett 12(9):5039–5047

30. Huang S, Fan F, Li J, Zhang S, Zhu T (2013) Stress generation during lithiation of high-capacity electrode particles in lithium ion batteries. Acta Mater 61(12):4354–4364

31. Ryu I, Lee SW, Gao H, Cui Y, Nix WD (2014) Microscopic model for fracture of crystalline Si nanopillars during lithiation. J Power Sources 255:274–282

32. Berla LA, Lee SW, Cui Y, Nix WD (2015) Mechanical behavior of electrochemically lithiated silicon. J Power Sources 273:41–51

33. Sethuraman VA, Chon MJ, Shimshak M, Van Winkle N, Guduru PR (2010) In situ measurement of biaxial modulus of Si anode for Li-ion batteries. Electrochem Commun 12(11):1614–1617

34. Amanieu H-Y, Aramfard M, Rosato D, Batista L, Rabe U, Lupascu DC (2015) Mechanical properties of commercial Mn2O4 cathode under different states of charge. Acta Mater 89:153–162

35. Tao X, Du J, Sun Y, Zhou S, Xia Y, Huang H, Gan Y, Zhang W, Li X (2013) Exploring the energy storage mechanism of high performance MnO2 electrochemical capacitor electrodes: an in situ atomic force microscopy study in aqueous electrolyte. Adv Funct Mater 23(37):4745–4751

36. Wang X, Sakiyama Y, Takahashi Y, Yamada C, Naito H, Segami G, Hironaka T, Hayashi E, Kibe K (2007) Electrode structure analysis and surface characterization for lithium-ion cells simulated low-earth-orbit satellite operation: I Electrochemical behavior and structure analysis. J Power Sources 167(1):162–170

37. Wang Y, Yan X, Bie X, Fu Q, Du F, Chen G, Wang C, Wei Y (2014) Effects of aging in electrolyte on the structural and electrochemical properties of the Li[Li0.18Ni0.15Co0.15Mn0.52]O2 cathode material. Electrochim Acta 116:250–257

38. Wang X, Hironaka T, Hayashi E, Yamada C, Naito H, Segami G, Sakiyama Y, Takahashi Y, Kibe K (2007) Electrode structure analysis and surface characterization for lithium-ion cells simulated low-earth-orbit satellite operation: II: Electrode surface characterization. J Power Sources 168(2):484–492

39. Liu P, Wang J, Hicks-Garner J, Sherman E, Soukiazian S, Verbrugge M, Tataria H, Musser J, Finamore P (2010) Aging mechanisms of LiFePO4 batteries deduced by electrochemical and structural analyses. J Electrochem Soc 157(4):A499–A507

40. Braithwaite JW, Gonzales A, Nagasubramanian G, Lucero SJ, Peebles DE, Ohlhausen JA, Cieslak WR (1999) Corrosion of lithium-ion battery current collectors. J Electrochem Soc 146(2):448–456

41. Xu J, Liu BH, Hu DY (2016) State of charge dependent mechanical integrity behavior of 18650 Lithium-ion batteries. Sci Rep 6:11

42. Xu J, Liu BH, Wang LB, Shang S (2015) Dynamic mechanical integrity of cylindrical lithium-ion battery cell upon crushing. Eng Fail Anal 53:97–110

43. Xu J, Liu BH, Wang XY, Hu DY (2016) Computational model of 18650 lithium-ion battery with coupled strain rate and SOC dependencies. Appl Energy 172:180–189

44. Tsutsui W, Siegmund T, Parab ND, Liao H, Nguyen TN, Chen W (2017) State-of-charge and deformation-rate dependent mechanical behavior of electrochemical cells. Exp Mech. https://doi.org/10.1007/s11340-017-0282-2

45. Liu YJ, Li XH, Guo HJ, Wang ZX, Hu QY, Peng WJ, Yang Y (2009) Electrochemical performance and capacity fading reason of LiMn2O4/graphite batteries stored at room temperature. J Power Sources 189(1):721–725

46. Petit M, Prada E, Sauvant-Moynot V (2016) Development of an empirical aging model for Li-ion batteries and application to assess the impact of vehicle-to-grid strategies on battery lifetime. Appl Energy 172:398–407

47. Jeong WT, Lee KS (2002) Electrochemical cycling behavior of LiCoO2 cathode prepared by mechanical alloying of hydroxides. J Power Sources 104(2):195–200

48. Osaka T, Nakade S, Rajamaki M, Momma T (2003) Influence of capacity fading on commercial lithium-ion battery impedance. J Power Sources 119:929–933

49. Yang L, Cheng X, Gao Y, Ma Y, Zuo P, Du C, Cui Y, Guan T, Lou S, Wang F, Fei W, Yin G (2014) Lithium deposition on graphite anode during long-term cycles and the effect on capacity loss. RSC Adv 4(50):26335–26341

50. Dahéron L, Dedryvère R, Martinez H, Ménétrier M, Denage C, Delmas C, Gonbeau D (2008) Electron transfer mechanisms upon lithium Deintercalation from LiCoO2 to CoO2 investigated by XPS. Chem Mater 20(2):583–590

51. Kim JH, Woo SC, Park MS, Kim KJ, Yim T, Kim JS, Kim YJ (2013) Capacity fading mechanism of LiFePO4-based lithium secondary batteries for stationary energy storage. J Power Sources 229:190–197

52. Fu R, Xiao M, Choe S-Y (2013) Modeling, validation and analysis of mechanical stress generation and dimension changes of a pouch type high power Li-ion battery. J Power Sources 224:211–224